

# Section 1

## PROGRESS IN LASER FUSION

### 1.A Production and Characterization of Hot, Long-Scale-Length Laser Plasmas

The production and characterization of long-scale-length laser plasmas are essential for the study of the laser-plasma interaction processes that are likely to occur in laser-fusion reactor targets. To carry out such experiments under true reactor conditions, i.e., in spherical geometry for direct-drive laser fusion, would require very large laser energies (comparable to reactor energies) that are presently unavailable. Research has therefore been concentrated on planar targets, with the goal of producing plasmas with scale lengths and electron temperatures as close as possible to those of reactor plasmas.

An extensive series of long-scale-length plasma experiments has been carried out on OMEGA. Thin plastic disks of finite diameter (600  $\mu\text{m}$ ) have been exploded using most of the 24 OMEGA beams to form plasmas with scale lengths close to 1 mm. By delaying in time some of the laser beams, electron temperatures  $\geq 1$  keV have been produced in plasmas of density around eighth critical and maintained over extended periods of time ( $\geq 1$  ns). This article describes the characterization of these plasmas by a variety of techniques, and shows that the two-dimensional (2-D) plasma expansion and the temporal evolution of the electron temperature and density are in close agreement with *SAGE* simulations. The plasma thus produced forms an excellent tool for investigating laser-plasma interaction processes under conditions relevant to future laser-fusion reactor targets.

Early long-scale-length plasma experiments were carried out using solid targets, with one or more laser beams overlapped onto a large spot of diameter up to 1 mm.<sup>1</sup> The density scale length achieved in this geometry, characterized simply as  $L_n = n_e/|\nabla n_e|$  where  $n_e$  is the electron density, initially increases with time during the laser pulse, but is eventually limited to some number of order unity times the beam diameter when an initially planar plasma flow develops into a divergent flow; laser energy delivered after this transition is relatively ineffective at increasing the plasma scale length. In the design of these experiments, the fundamental limitation is the available laser energy. If the beam diameter is to be increased with the laser intensity maintained constant, the laser power must be increased in proportion to the beam area; also, the laser duration must be increased, roughly in proportion to the beam diameter, since it will take longer to establish the greater scale length. The energy required thus scales as the cube of the beam diameter. The alternative of reducing the laser intensity while the beam diameter and pulse width are increased would lead to plasmas with unacceptably low electron temperatures ( $\ll 1$  keV) for interaction-physics experiments relevant to reactor plasmas.

Some improvement is available through replacing the solid target by a thin-foil target, which is exploded as a result of irradiation from one or both sides.<sup>2-4</sup> Here, after the laser beam(s) burn through the target, a density profile is obtained that has a maximum in the center. The density scale length  $L_n$  as previously defined is infinite in the center, and can be made as large as desired by looking sufficiently close to the center. However, many convective processes (such as filamentation) require that the laser propagate through a significant length of plasma, and for a reasonable comparison to be made with (thick) solid targets it is conventional to define the scale length of the exploding-foil plasma  $L_p$  as the FWHM of the density profile, usually measured along the initial target normal. The density profile of an exploding foil differs from that of a direct-drive reactor target in that it has a density maximum but no critical surface at times of interest; however, its characteristics are otherwise generally considered to be sufficiently close to those of reactor plasmas to be of interest. As with the solid target, the scale length of the thin-foil target is limited by the beam diameter for the same reason of divergent flow. However, since the foil expands in both directions, a larger scale length for a given beam diameter might be expected using a foil.

All of the experiments cited so far suffer from a disadvantage that the laser beams serve the dual purposes of forming and interacting with the plasma. They are defocused to a large spot diameter to form the plasma, and so the desired intensities for studying nonlinear laser-plasma interactions (typically up to a few times  $10^{15}$  W/cm<sup>2</sup>) may not be available. Additionally, systematic experimentation is difficult since changing the laser intensity desired for a particular interaction-physics experiment will simultaneously change the plasma conditions. This problem has been mitigated by making appropriate adjustments to the laser-beam diameter and pulse width in order to produce a plasma of approximately constant hydrodynamic conditions over a broad range of laser intensities.<sup>3,4</sup> However, an alternate solution is

often preferred. This involves first irradiating a target with a low-intensity, large-diameter plasma-generation beam and then, after the plasma has expanded sufficiently to reach the appropriate density, irradiating the pre-formed plasma with a high-intensity, tightly focused interaction beam. This technique was first employed using solid targets<sup>5</sup> and has subsequently been used almost exclusively with exploding foils. These latter experiments have been carried out in two distinct geometries: cylindrical<sup>6,7</sup> and line focus.<sup>8</sup> In the first geometry the plasma-generation beam is usually focused to a circular spot with the largest possible diameter, and the interaction beam is incident approximately parallel to the plasma-generation beam. In the second geometry the plasma-generation beam is focused along a line, with the line length equal to the desired scale length, and the interaction beam is incident orthogonally, i.e., along the line focus. This latter geometry has the advantage that a long scale length can be produced with a plasma-generation beam of modest energy; however, the expanded plasma, which is approximately cylindrical about the axis of the interaction beam, is subject to strong transverse density gradients. Alignment of the interaction beam is thus made difficult due to refraction, and the homogeneity of the plasma seen by the interaction beam is harder to ensure.

While many of these experiments have successfully accessed plasma conditions not currently available in spherical geometry, both cylindrical and line-focus geometries suffer from a limited ability to simultaneously achieve the desired plasma density and temperature, often leading to plasma electron temperatures well below 1 keV at the time of the interaction beam. This occurs for at least three reasons: (a) the plasma-generation beam is necessarily defocused to a low intensity; (b) the plasma cools during expansion to the desired density; and (c) as the plasma expands to densities significantly below critical, inverse-bremsstrahlung absorption of laser energy becomes progressively less effective. In spite of this problem, such plasmas do form a useful test-bed for plasma-physics experiments; in particular, they are strongly perturbed by the interaction beam and are subject to strong self-focusing (thermal and/or ponderomotive). However, for greater relevance to reactor plasmas, higher temperatures are required. Additionally, for a clean interaction-physics experiment, it is generally desirable that the interaction beam cause minimal hydrodynamic perturbation to the plasma. One solution to this problem is to use multiple laser pulses for plasma generation and heating, staggered in time; for example, Batha *et al.*<sup>7</sup> irradiated 15- $\mu\text{m}$ -thick CH foils with five NOVA beams at time  $t = 0$ , followed by four more beams at  $t = 1.3$  ns and one tightly focused interaction beam at  $t = 2.7$  ns, with 1–2 kJ per beam.

In the current experiments the OMEGA laser has been used to produce hot, long-scale-length plasmas that are approximately isothermal at the interaction time. This has been achieved by exploding the foil with a subset of the 24 beams and, after an appropriate time delay, using another subset to maintain the temperature of the expanding plasma. In this respect, the experiment is similar to that of Ref. 7. Furthermore, the choice of a mass-limited target, typically a 6- $\mu\text{m}$ -thick CH foil whose diameter (600  $\mu\text{m}$ ) is

matched to the focal diameter of the plasma-generation beams, allows for optical probing of the central region of the plasma, a region that has been obscured by the unirradiated portion of the target in similar experiments using large thin foils. In addition, the plasma created in this way can be nearly spherically symmetric, thus allowing the introduction of the interaction beam from different directions and opening the possibility for conducting experiments with overlapping interaction beams. A further feature of this configuration is that some of the delayed subset of beams can be infrared (1054 nm) in order to provide more efficient heating of the expanding plasma if densities below  $10^{21} \text{ cm}^{-3}$  (the critical density at 1054 nm) are desired. The OMEGA system also allows for the inclusion of beam-smoothing techniques such as phase plates<sup>9</sup> or smoothing by spectral dispersion (SSD),<sup>10</sup> although most of the results here were obtained without SSD. Typical plasmas produced in the current experiments have center densities around  $n_c/8$ , and are maintained within a factor of two of this density and at a temperature  $T_e \geq 1 \text{ keV}$  for approximately 1 ns, with scale lengths  $L_p$  of 0.5–1 mm. (Throughout this article  $n_c$  indicates the critical electron density for a laser wavelength of 351 nm, i.e.,  $9 \times 10^{21} \text{ cm}^{-3}$ .)

In this article the experimental conditions and diagnostics are first described in detail. Simulations using the 2-D Eulerian hydrodynamics code *SAGE*<sup>11,12</sup> are discussed in the following section. Experimental results are then presented for the electron temperature measured spectroscopically as a function of time, for the electron density inferred from stimulated Raman scattering (SRS) spectra, and for the 2-D evolution of the plasma as indicated by optical probing. In all cases, it is seen that the experimental results agree well with the predictions of the hydrodynamic simulations. The main conclusion is that these long-scale-length plasmas are well characterized and well suited to interaction-physics experiments of relevance to laser-fusion reactors.

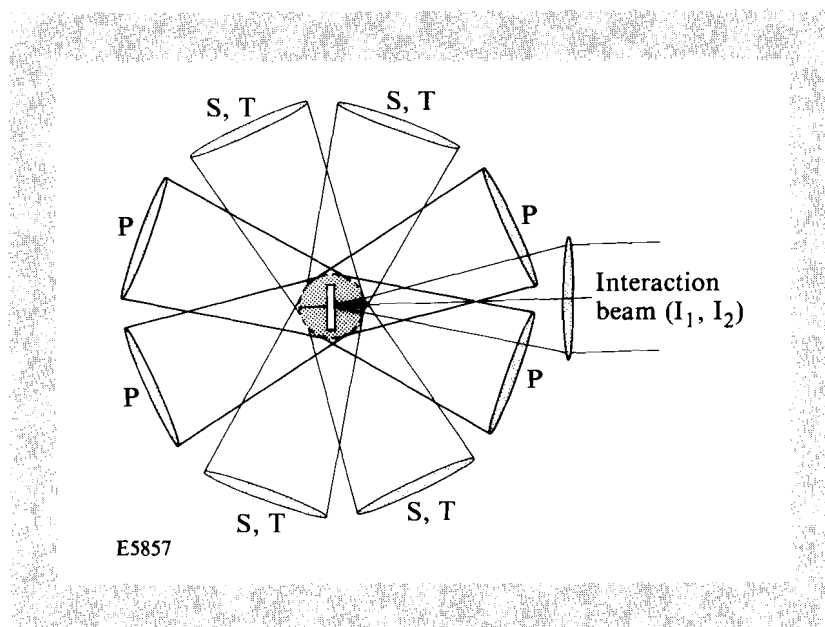
### Experimental Conditions and Diagnostics

The target irradiation configuration is shown in Fig. 47.1. Two sets of four opposing beams (P) are used to explode the foil. The on-target laser energy is typically 50–60 J per beam with a pulse duration of ~0.60–0.65 ns at a wavelength of 351 nm. On each side, the four primary plasma-producing beams are surrounded by eight other beams, of which four are used as secondary heating beams, incident 0.6 ns after the primary beams, and three can also irradiate the target as tertiary beams, peaking typically 1 ns after the primary beams. The remaining beam from one side is rerouted to become the interaction beam. Throughout this article the primary beams peak at 1.0 ns, the secondaries at 1.6 ns, and the tertiaries at 2.0 ns. The interaction beam has been located at 1.6 ns in some experiments and at 2.2 ns in others. All beams have a wavelength of 351 nm, except the tertiary beams whose wavelength is 1054 nm.

All primary and secondary beams (but not the tertiary beams) are outfitted with distributed (random) phase plates (DPP's)<sup>9</sup> in front of the focusing lens ( $f = 60 \text{ cm}$ ) to produce an Airy envelope for the intensity distribution in the

Fig. 47.1

Target irradiation configuration. Schematic layout of  $2 \times 4$  primary plasma-producing beams (P),  $2 \times 4$  secondary (S) and 6 tertiary (T) heating beams, and one interaction beam with two possible timings ( $I_1, I_2$ ). The interaction beam is tightly focused onto the target (spot diameter  $\approx 90\text{-}\mu\text{m}$  FWHM), while all other beams are strongly defocused (spot diameter  $\approx 450\text{-}\mu\text{m}$  FWHM). All beams have wavelength  $351\text{ nm}$  with  $\geq 60\text{ J/beam}$  on target, except the tertiary beams that have wavelength  $1054\text{ nm}$  and  $\geq 100\text{ J/beam}$ . The pulse duration of the UV beams is  $600\text{--}650\text{ ps}$ .



focal plane of the lens. The  $1.25\text{-mm}$ -diam hexagonal cells of the DPP result in focal spots of  $\sim 163\text{-}\mu\text{m}$  FWHM. However, the primary and secondary beams are focused  $1.65\text{ mm}$  past the target surface to produce a spot diameter of  $\sim 450\text{-}\mu\text{m}$  FWHM. With this focusing, sufficient laser-beam intensity irradiates the edge of the  $600\text{-}\mu\text{m}$ -diam target to explode and heat it with a reasonable degree of uniformity, although simulations show the center to expand faster than the edge. The resulting intensities in the primary and secondary heating beams place them below most of the thresholds for nonlinear interaction processes, as has been verified by null experiments without the interaction beam. The wavelength, pulse duration, and energy of the interaction beam are the same as those of the primary beams, but the DPP cell sizes are twice as large ( $2.5\text{-mm}$  diameter) so that the spot size at best focus is a factor of two smaller. The interaction beam is focused at the center of the target.

Equivalent-target-plane photographs have shown that the envelope of the interaction beam matches well with the predicted Airy envelope  $[4J_1^2(x)/x^2]$ , which has an FWHM of  $82\text{ }\mu\text{m}$  and a radius to the first zero of  $97\text{ }\mu\text{m}$ . The Airy envelope is very close to a Gaussian of the same FWHM. The peak (on-axis) intensity of the envelope is found to be  $\sim 1.2 \times 10^{15}\text{ W/cm}^2$  (for a  $60\text{-J}$  beam). The intensity distribution is strongly modulated by the speckle pattern produced by the DPP's, but only  $\sim 2\%$  of the beam energy is found to be above  $1.5 \times 10^{15}\text{ W/cm}^2$ . However, some speckle may be present with a spatial scale of less than the minimum  $10\text{ }\mu\text{m}$  that was experimentally resolved.

The primary and secondary beams, which are focused to a plane intermediate between the near field and the far field, are less well characterized, but are approximated by Gaussians of  $450\text{-}\mu\text{m}$  FWHM. Diffraction calculations and idealized geometric focusing calculations both suggest an azimuthally

averaged profile with  $\text{FWHM} \approx 430 \mu\text{m}$  and an envelope a bit flatter than a Gaussian, assuming a flat distribution of radius 8 cm at the focus lens. As in the case of the interaction beam, a strong speckle pattern is present caused by the DPP's, but the presence of overlapping primary and secondary beams diminishes the high contrast of the speckle pattern to some extent.

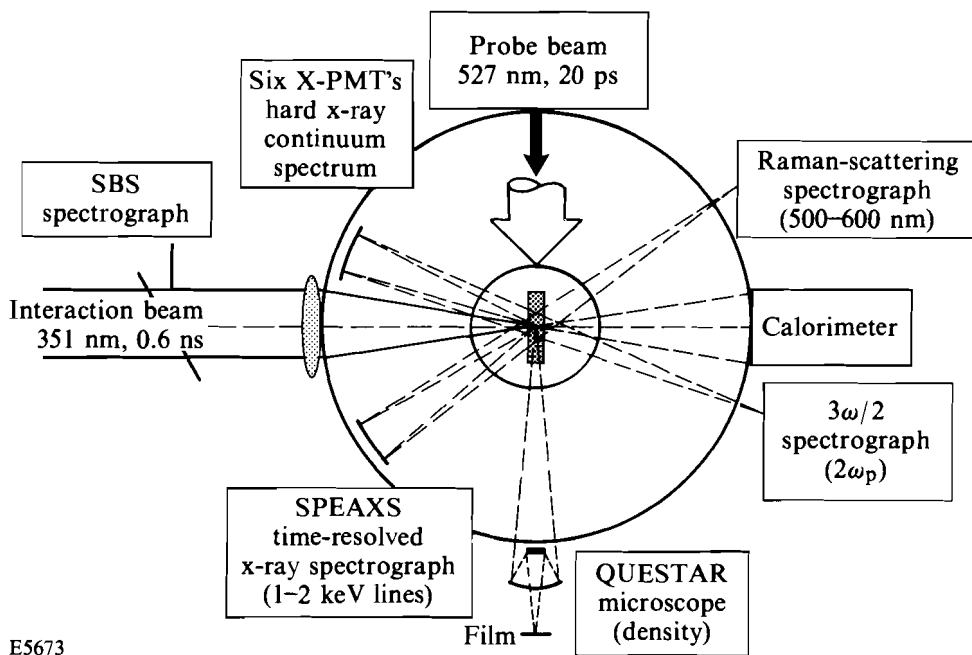
After the initial explosion of the foil, thermal conduction is expected to render the plasma density and temperature profiles very smooth by the time the interaction beam is switched on. This process is particularly effective in the presence of the secondary heating beams that help to maintain electron temperatures of greater than 1 keV over nearly 1 ns; in this case speckle in the interaction beam of scale  $< 10 \mu\text{m}$  should be well smoothed out by thermal conduction.

In all these experiments the targets were free-standing CH foils,  $600 \mu\text{m}$  in diameter and  $6 \mu\text{m}$  thick, mounted on  $\sim 10\text{-}\mu\text{m}$ -diam glass stalks. Some targets contained a central Al signature layer of  $\sim 1000\text{-}\text{\AA}$  thickness for x-ray spectroscopy and temperature diagnosis. In addition, all targets were overcoated with  $500 \text{\AA}$  of Al in order to eliminate or reduce shinethrough effects,<sup>13</sup> i.e., to prevent laser light from penetrating into the target interior prior to plasma formation at the target surface.

The diagnostics employed for these experiments are shown schematically in Fig. 47.2. There were two primary plasma diagnostics, a time-resolved x-ray spectrograph used to determine the electron temperature, and a short

Fig. 47.2

Schematic layout of diagnostics. The polarization of the interaction beam is roughly perpendicular to the plane of the paper; the  $3\omega/2$  collection mirror is actually located above the interaction beam so as to lie approximately within the plane of polarization.



E5673

527-nm optical probe beam used in conjunction with a microscope to diagnose the low-density plasma evolution by means of Schlieren photography. In addition, a 1/4-m spectrograph was used to obtain time-integrated visible spectra of the SRS arising from variously timed interaction beams; since SRS is a nonlinear function of laser intensity, this diagnostic provided density measurements in the vicinity of one-tenth critical with some time resolution. The remaining diagnostics were aimed at diagnosing other nonlinear processes such as the two-plasmon decay instability ( $3\omega/2$  emission, time-integrated UV spectroscopy), and stimulated Brillouin scattering (SBS, time-integrated UV spectroscopy). Data from these nonlinear processes are presented here only to the extent that they relate to plasma diagnosis. In addition, two channels of *K*-edge-filtered, hard-x-ray photomultipliers were used for fast-electron diagnostics, and the transmitted light within the original cone of the interaction beam was measured using a calorimeter.

The two-plasmon-decay diagnostic, a 1/4-m spectrograph detecting radiation in the vicinity of  $3\omega/2$  (i.e., 234 nm), had its collection mirror in the plane of polarization of the interaction beam (perpendicular to the plane of the drawing), but for ease of graphic representation it is shown otherwise. The stimulated Raman spectra were collected out of the plane of polarization and at  $\sim 45^\circ$  to the interaction beam in the backscatter direction. Both of the SRS and  $3\omega/2$  collection optics were *f*/8 spherical mirrors, with either an aluminum coating (for SRS) or a dielectric coating (for  $3\omega/2$ ). Stimulated Brillouin backscattering of the interaction beam was monitored using a diagnostic pick-off with 4% reflection placed in the path of this beam.

The time-resolved x-ray spectroscopy was carried out using the streaked x-ray crystal spectrograph SPEAXS<sup>14</sup> in conjunction with a PET crystal that allowed convenient registration of the Ly $\beta$  and He $\beta$  lines of Al with better than 50-ps resolution. A 1000-Å-Al signature layer embedded in the midplane of the target was used to determine the electron temperature evolution using the time-dependent intensity ratio of the Ly $\beta$  to the He $\beta$  line. Typical time-resolved spectra are shown in Fig. 47.3 for two cases. In Fig. 47.3(b) the x-ray spectrum is shown for a target without the central Al layer. The outer 500-Å-Al layer is seen to light up early on in the pulse. Doppler splitting in the spectral lines is evident; this occurs because the front and rear sides expand in opposite directions (with velocities  $\sim 10^8$  cm/s). When a central Al signature layer is employed [Fig. 47.3(a)], strong and long-lasting hydrogen- and helium-like emission is observed. While some Doppler broadening is observed, there is no Doppler splitting from the central Al layer, since this layer always has its highest density (and main emission region) at the center of the plasma where the flow velocity is zero. Figure 47.4 shows intensity-converted line-outs along the time axis for the Ly $\beta$  and He $\beta$  lines of Fig. 47.3(a), obtained using the calibration data of Ref. 14.

The temporally varying intensity ratio of the Ly $\beta$  and He $\beta$  lines is indicative of the temperature evolution in the plasma. For a given electron density ( $n_e$ ) and temperature ( $T_e$ ) this ratio can be calculated using the atomic

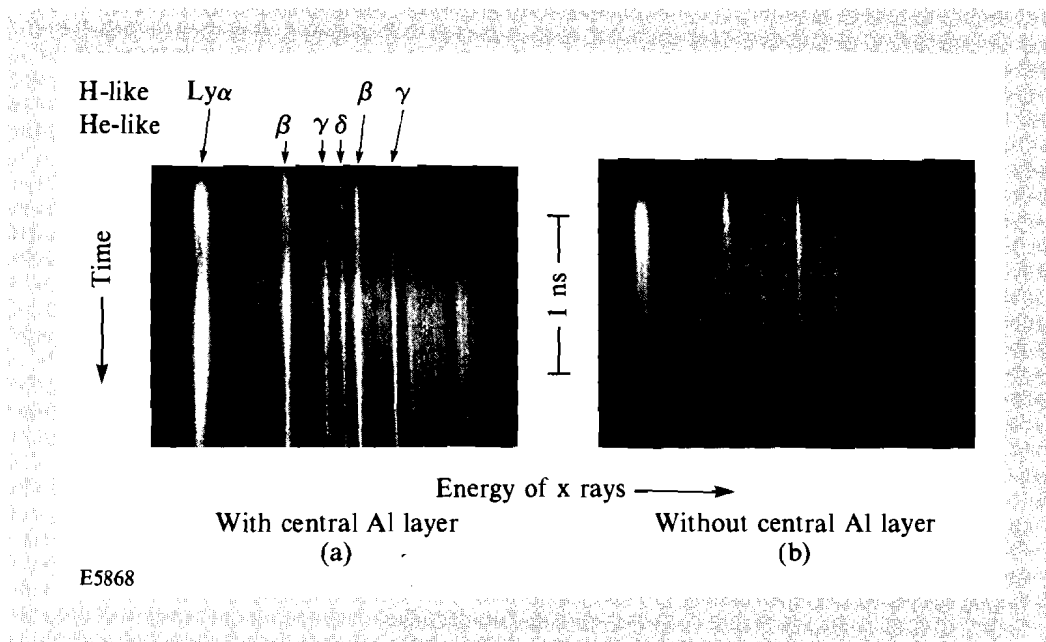


Fig. 47.3  
Time-resolved x-ray streak spectra from SPEAXS in the vicinity of the aluminum He $\beta$  and Ly $\beta$  lines. (a) 6- $\mu\text{m}$ -thick CH target with a 500- $\text{\AA}$ -Al barrier layer on each side and a central 1000- $\text{\AA}$ -Al signature layer; (b) same target but without the signature layer.

rate-equation code POPION.<sup>15</sup> This code uses a detailed-configuration, screened hydrogenic-ion model in a set of multispecies, collisional-radiative rate equations that are solved to obtain the ion species and the required level populations. It is found that the line ratio is only a weak function of  $n_e$ ; e.g., a factor-of-4 error in  $n_e$  typically results in only a  $\sim 10\%$  change in the value of  $T_e$  corresponding to a given line ratio. Thus, with a reasonable estimate of  $n_e$ , the time-dependent electron temperature can be obtained from Fig. 47.4. This method is especially applicable to emission from the center of the target, since the following experimental results support the *SAGE* predictions for the electron density there. However, it is harder to infer the temperature of the outer Al layer at early times since, in this case, the density of the radiating Al is less well known.

The optical probe beam was used to characterize the overall plasma shape and dimension. The choice of a frequency doubled (as opposed to quadrupled) beam resulted in an enhanced sensitivity to low-density regions. The pulse duration was  $\sim 20$  ps and the synchronization was monitored using fast diodes and a Hewlett-Packard time-interval counter. For some of the experiments a pulse-stacked probe beam was used. This was generated by placing two 70%-reflecting mirrors in the path of the optical probe.

The probe beam was used to take dark-field images of the plasma using light scattered or refracted by the plasma. A 4-in.-diam QUESTAR<sup>®16</sup> model QM1 was used as a microscope with a long working distance ( $\sim 1$  m). The central stop (the secondary mirror of the Cassegrainian telescope) also serves as a beam stop for the dark-field photography. The 2-cm diameter of the beam stop gives a lower cutoff angle corresponding to  $\sim f/50$ , and the edge of the outer mirror results in an upper cutoff at  $f/11$ . For the experiments using the pulse-stacked beam, an enlarged central stop was used whose

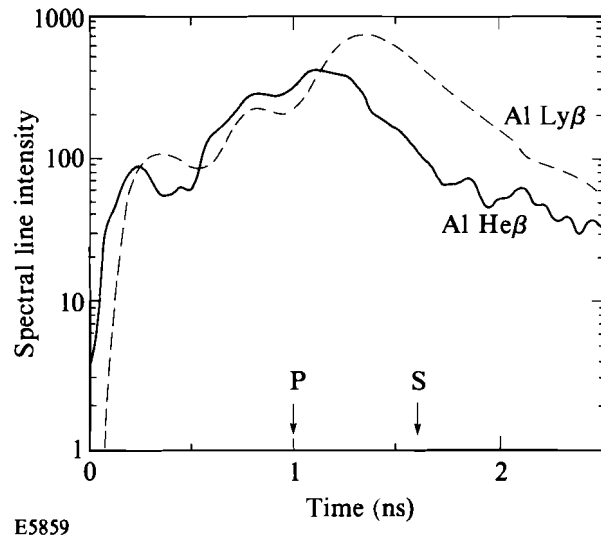


Fig. 47.4  
Line-out along the time axis for the He $\beta$  and Ly $\beta$  lines for case (a) of Fig. 47.3; P and S indicate the peaks of the primary and secondary beams.

dimensions ( $f/14$ ) differed only slightly from the instrument's entrance aperture. This arrangement resulted in images of only very narrow regions of the plasma, and enabled nonoverlapping multiple exposures of the expanding plasma to be obtained on a single shot, with a precise relative timing, in order to accurately characterize the expansion phase of the plasma.

### Two-Dimensional Hydrodynamic Simulations

These experiments have been extensively simulated using *SAGE* in 2-D cylindrical geometry. In order to illustrate the main hydrodynamic features of the formation of typical long-scale-length plasmas, the discussion will focus on a representative simulation with all beams included. The parameters for this simulation, chosen to correspond to one experimental shot discussed below, are summarized in Table 47.I.

The wavelength, pulse width, and timing of the various beams correspond to the standard experimental conditions described in the previous section, with the interaction beam at the later time of 2.2 ns. All UV beams used DPP's and were modeled as spatial Gaussians with the appropriate diameters at half-maximum intensity  $d_{FWHM}$ . This is a very good approximation to the ideal Airy profile of the beam envelope. The diameters  $d_{90}$  containing 90% of the energy in the Gaussian profile are also given in Table 47.I. Since these diameters correspond to an intensity 10% of the maximum, the 600- $\mu\text{m}$ -diam targets are well irradiated by the primary and secondary beams for which  $d_{90} = 820 \mu\text{m}$ . For computational efficiency, the spatial profile is truncated at a radius  $d_{90}/2$ , and the stated energy is delivered within this radius. The peak intensity per beam, defined as the intensity at the peak of the beam in time and at radius  $r = 0$ , is  $3.9 \times 10^{13} \text{ W/cm}^2$  for each of the primary and secondary beams and  $9.5 \times 10^{14} \text{ W/cm}^2$  for the interaction beam. Laser-energy deposition is modeled using three-dimensional (3-D) ray tracing.

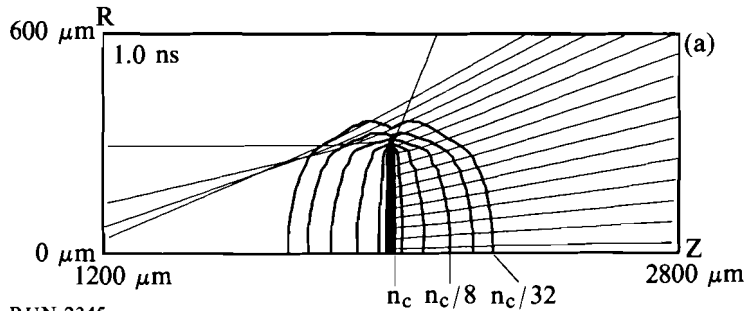
Table 47.I: Parameters of SAGE simulation with all beams included.

	Primary	Secondary	Tertiary	Interaction
Wavelength (nm)	351	351	1054	351
Temporal FWHM (ns)	0.6	0.6	0.6	0.6
Time of peak (ns)	1.0	1.6	2.0	2.2
Number of beams	4/side	4/side	2/side	1 from right
Energy	200 J/side	200 J/side	150 J/side	50 J
Spatial profile	Gaussian	Gaussian	Flat	Gaussian
Diameter $d_{\text{FWHM}}$ ( $\mu\text{m}$ )	450	450	2000	90
Diameter $d_{90}$ ( $\mu\text{m}$ )	820	820	–	160
Peak intensity per beam ( $\text{W}/\text{cm}^2$ )	$3.9 \times 10^{13}$	$3.9 \times 10^{13}$	$3.3 \times 10^{12}$	$9.5 \times 10^{14}$
Beam geometry	f/0.87 cone	Skew rays at $\theta_i=69^\circ$	Skew rays at $\theta_i=69^\circ$	Parallel beam
Number of rays	15	$7 \times 4$	$7 \times 4$	15
Absorption (%)	77	48	19	40

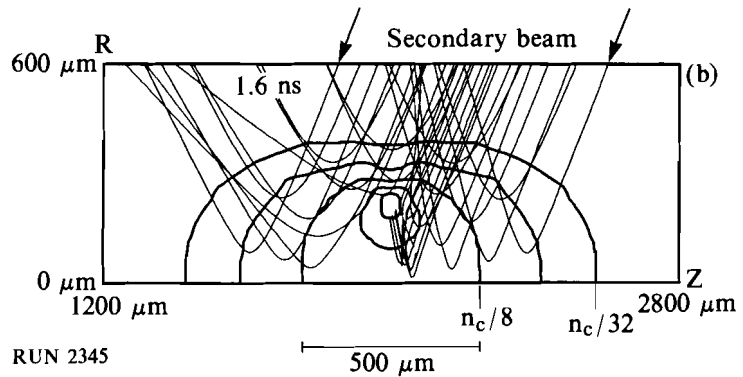
TC 3011

For computational efficiency, the CH is treated as a fully ionized perfect gas, omitting equation-of-state and radiation effects. For such low- $Z$  material, which is fully ionized at all times except very early in the interaction, this has been found to be a very good approximation. No attempt has been made to model the 1000-Å-Al signature layer in the targets used for spectroscopic diagnostics. This layer, when fully ionized, contains the same number of electrons per unit area as only  $0.23 \mu\text{m}$  of CH (i.e., 4% of the target thickness), and is therefore unlikely to significantly perturb the hydrodynamics. The simulation employs an orthogonal grid, with 40 points up to a radius of  $1600 \mu\text{m}$  and 85 points over  $4000 \mu\text{m}$  in the  $z$  direction. The initial target location is at  $z = z_{\text{mid}} = 2000 \mu\text{m}$ .

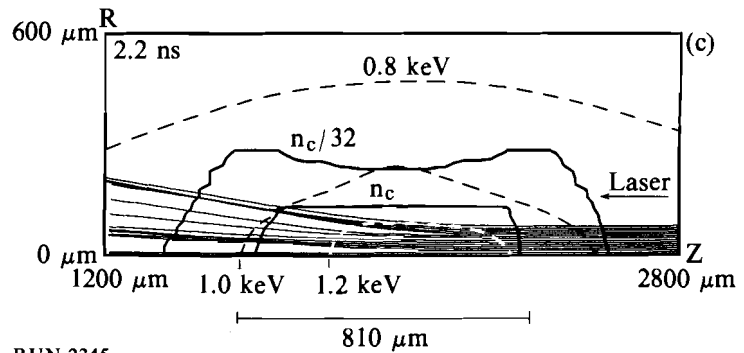
Results from this simulation are shown at three successive times in Fig. 47.5(a)–(c), corresponding to the peaks of the primary, secondary, and interaction beams. At the time of the peak of the primary beams [Fig. 47.5(a)] the plasma is still overdense and strongly absorbing. Note that only the rays incident from the right are shown, with the ends of the rays marking the 90% absorption point. The outermost rays correspond to the truncation radius of  $d_{90}/2$ . All four overlapping primary beams are represented as a single beam with a broad f/0.87 cone, corresponding to a maximum angle of incidence of  $30^\circ$ . (In the OMEGA geometry, the four beams are each  $\sim f/3.5$  cones incident at  $30.4^\circ$ .) This representation appears to be reasonable, as refraction is clearly seen to be unimportant (except for the occasional ray that strikes the edge of the target) and there are no problems associated with the



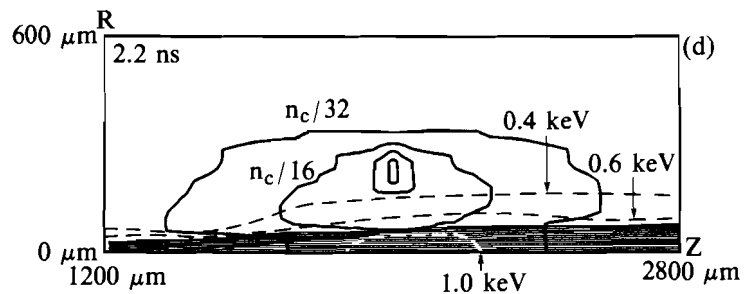
RUN 2345  
TC2932



RUN 2345  
TC2933



RUN 2345  
TC2934



RUN 2344  
TC2935

Fig. 47.5

Isodensity contours of the expanding plasma, from a simulation with all beams on, at three successive times: (a)  $t = 1.0$  ns, the peak of the primary plasma-producing beams; (b)  $t = 1.6$  ns, the peak of the secondary heating beams; and (c)  $t = 2.2$  ns, the peak of the interaction beam. In each case typical ray trajectories (from the right side only) are shown for the beam peaking at that time. In case (c), contours of electron temperature are also shown (dashed lines) and indicate a nearly isothermal plasma. The plot shown in (d) is as in (c) but for a different simulation, without the secondary and tertiary beams; here the plasma is significantly perturbed by the interaction beam and high temperatures are found within a long and narrow channel.

geometric foci that lie well beyond the plasma; the main function of the primary beams is to deposit energy on or near the surface of the target. The main shortcoming of this representation is probably the (weakly) 3-D nature of the actual irradiation configuration, where the target-plane irradiation pattern is based on the superposition of two ellipses of aspect ratio  $\cos(30.4^\circ)$  with their major axes orthogonal. The pattern produced by each set of four primary beams has the same orientation; thus, in the azimuthal direction around the  $z$  axis, one should expect to find four regions of somewhat under-irradiated plasma. Just 15 rays per timestep are sufficient to give smooth and convergent plasma behavior. This is made possible by the algorithm whereby *SAGE* deposits ray energy in an area-weighted manner among the four cells nearest each deposition point on the trajectory;<sup>17</sup> thermal diffusion also smooths out residual small-scale deposition nonuniformities.

Figure 47.5(b) shows the corresponding isodensity contours at the peak of the secondary heating beams. The plasma is now underdense and already possesses acceptable characteristics for long-scale-length interaction experiments. Along the axis the peak electron density is  $n_e \approx n_c/4$ , the electron temperature is  $T_e \geq 1$  keV, and the density scale length is  $L_p \approx 500 \mu\text{m}$ . The density contours show an essentially spherical plasma, well matched to the obliquely incident secondary beams, except for the doughnut-shaped region of high density off axis. This results from the preferential expansion along the axis due to the center-peaked spatial profile of the primary beams. For a while the secondary beams are deflected away from the center of the plasma by this high-density region. It should be noted that the secondary beams are modeled as a cylindrical bundle of parallel rays, incident at  $69^\circ$  to the  $z$  axis. Most of these rays thus follow 3-D trajectories that do not lie in the  $(r,z)$  plane, and so it is the  $r$  and  $z$  components of the trajectories that are plotted in Fig. 47.5(b).

At the peak of the interaction beam [Fig. 47.5(c)], the maximum on-axis electron density is one-eighth critical and the scale length  $L_p \approx 810 \mu\text{m}$ : within this distance,  $n_e$  varies between  $n_c/8$  and  $n_c/16$ . It is apparent from the simulation that the interaction beam does not significantly perturb this plasma (this will be quantified later in this article). Furthermore, no evidence of thermal self-focusing is seen, and the plasma deflects the interaction-beam rays outward. This is consistent with the hydrodynamic simulations of Ref. 17 where an example was given of the suppression of thermal self-focusing in a hot, long-scale-length plasma. In Fig. 47.5(c) electron temperature contours are overlaid (dashed lines) and the plasma is seen to be approximately isothermal. Over the whole  $810\text{-}\mu\text{m}$  scale length, the interaction beam sees a temperature of  $1.0\text{--}1.3$  keV. The parameters of this plasma should be well suited to interaction-physics experiments.

In order to illustrate the importance of the secondary beams in maintaining a hot plasma, a comparison simulation was carried out with just the primary and interaction beams included. Density and temperature contours for this case are shown in Fig. 47.5(d), at the same time as for Fig. 47.5(c). Here, in

contrast to Fig. 47.5(c), the interaction beam heats a long and narrow cylindrical region in the (moderately) cold preformed plasma, forming a low-density channel that in turn causes the interaction beam to focus (somewhat) to the left of the figure. In broad terms this process may be described as self-focusing, although the region of maximum refraction (near  $z = 2000 \mu\text{m}$ ) is spatially distinct from the focus. In Fig. 47.5(d) the focusing is very weak and not all rays are significantly bent. The locations of the foci vary in time, and a significant increase in the local electron temperature is not seen. The  $n_e/32$  contour, however, is somewhat perturbed in the focusing region.

It is evident from Fig. 47.5(c) that the peak temperature and density along the axis are representative of the conditions that the interaction beam sees. By plotting these quantities as a function of time the respective roles of the primary and secondary beams become apparent (Fig. 47.6). The time history of the peak on-axis electron temperature is shown [Fig. 47.6(a)] for four cases ranging from just the primary beams (P) to all beams (P + S + T + I). It is seen that the secondary beams (S) provide substantial plasma heating, and the interaction beam (I) provides some additional heating. On the other hand, the IR tertiary beams (T) clearly provide little heating in this simulation.

One interesting feature of this figure is the delay between the peak of the secondary beams (1.6 ns) and the resulting peak of electron temperature (1.8 ns, for curve P + S). This occurs because, at 1.6 ns, the secondary-beam rays are deflected away from the axis as previously noted in the discussion of Fig. 47.5(b).

The time history of the maximum on-axis electron density for the same four cases [Fig. 47.6(b)] shows a plasma expansion that is at first rapid and then slows down, as has been found in experiments and simulations elsewhere.<sup>3</sup> The main observation here is that the expansion history is determined largely by the primary beams with only minor differences between the four cases. Generally, the density falls faster at late times for the cases where the plasma is heated by extra laser beams, as might be expected. The bump at 2 ns is due to the off-axis doughnut-shaped region of high density “imploding” onto the axis when irradiated by the secondary beams, and does not occur in the case of primary beams only. The exact shape of this bump undoubtedly depends on the symmetry of the irradiation pattern and the resulting off-axis high-density torus. For the small number of beams used in the experiment this symmetry is likely to be far from perfect, as previously discussed, and the bump at 2 ns may actually only be observed as a flat density plateau. In any case, this off-axis region serves as a source of mass that helps maintain the peak on-axis density against what would otherwise be a more rapid decay.

## Experimental Results

### 1. Electron Temperature

One of the distinguishing characteristics of the background plasma formed in these experiments is the extended hot phase of the expanding plasma. This is generally difficult to achieve with laser systems of limited output energy. As is apparent from Fig. 47.6(a), the temporal staggering of

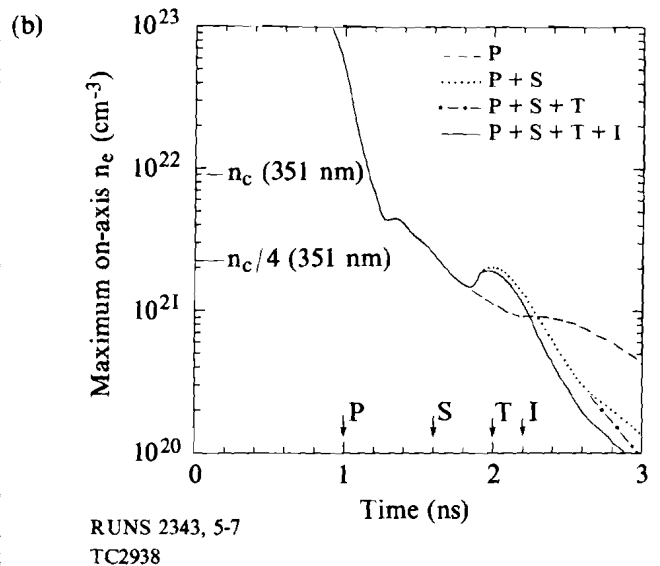
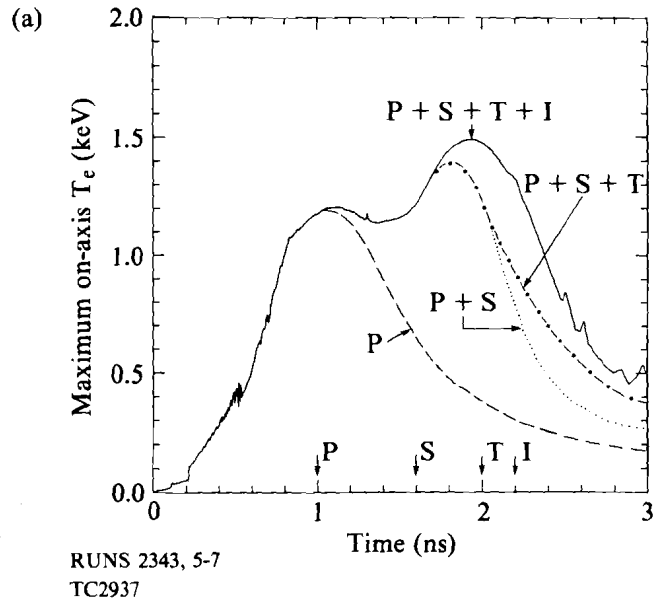
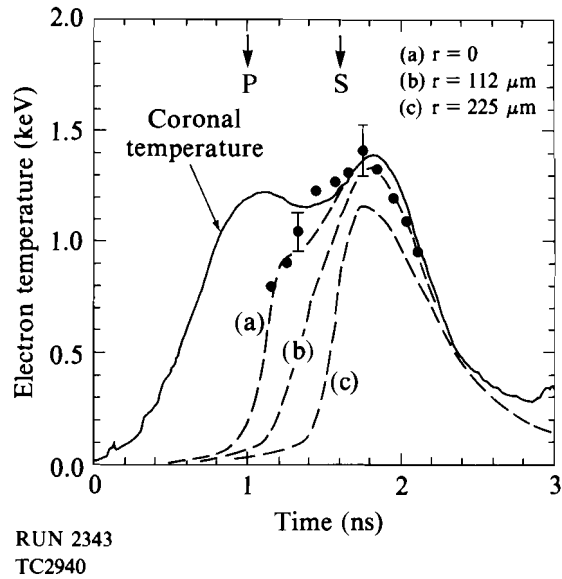


Fig. 47.6  
Maximum on-axis electron temperature (a) and density (b) for four cases: (P) primary beams only; (P + S) primary and secondary beams; (P + S + T) primary, secondary and tertiary beams; and (P + S + T + I) all beams.

the various OMEGA beams provides the necessary flexibility. Experimental confirmation has been obtained using targets that included a 1000-Å-Al signature layer in the center of the 6- $\mu\text{m}$ -thick CH disk. Using the temporally resolved x-ray line intensities of the aluminum Ly $\beta$  and He $\beta$  lines [Figs. 47.3(a) and 47.4] along with the temperature dependence of the Ly $\beta$  to He $\beta$  line ratio calculated by POPION, electron temperatures of 0.8–1.5 keV have been inferred over a period of  $\sim 1$  ns, as shown in Fig. 47.7. The experimental points in this figure start at  $\sim 1$  ns because it is at this time that the primary laser

Fig. 47.7

Temporal dependence of the electron temperature as measured by a central 1000-Å-Al layer embedded in the 6-μm-thick CH foil, for a shot with just primary and secondary beams. The experimental points were obtained from the streaked spectra of Fig. 47.3(a) using line ratios calculated by POPION. The solid line indicates two-dimensional *SAGE* predictions for the coronal temperature, defined as the maximum electron temperature along the  $z$  axis. The dashed lines indicate predictions for the electron temperature at (a)  $r = 0$ , (b)  $r = 112 \mu\text{m}$ , and (c)  $r = 225 \mu\text{m}$ , at the value of  $z$  ( $z_{\text{mid}}$ ) corresponding to the center of the target.



beams have burnt through to the signature layer: at earlier times the line emission is dominated by the 500-Å-thick outer barrier layers, also made of aluminum (see Fig. 47.3).

The dashed curve (a) indicates the electron temperature at the center of the target ( $r = 0$ ) and the solid line the maximum on-axis electron temperature calculated by *SAGE*. The latter temperature is labeled the “coronal” temperature because, early in time, before the primary beams have burnt through to the signature layer, the maximum occurs in the corona rather than at the center of the target. At later times the two calculated temperatures are almost indistinguishable. As expected, the experimental temperatures follow the predicted target-center temperatures early in time. The experimental measurements should correspond to a spatial average over the aluminum in the plasma, and therefore be somewhat lower than on-axis predictions, but this is believed to be a small effect because the plasma is predicted to be fairly close to isothermal. To illustrate this, the dashed curves (b) and (c) give the calculated electron temperature at  $r = 112 \mu\text{m}$  and at  $r = 225 \mu\text{m}$ , the latter being the half-maximum radius of the laser-intensity profile; burnthrough at these radii is somewhat delayed with respect to the axis, as expected, but later in time all calculated curves merge. It should be noted that the SPEAXS data did not have an independent timing fiducial for this series of experiments, so that the experimental data was shifted along the time axis to obtain the best fit. The error bars (approximately 10%) shown in this figure are indicative of the error with which the intensity ratio of the two x-ray lines can be determined, as well as the uncertainty in electron density (on which the line ratio is weakly dependent) as previously discussed. The close agreement between simulation and experiment provides evidence that the secondary beams do indeed maintain the plasma temperature.

## 2. Electron Density via Stimulated Raman Scattering

Stimulated Raman scattering was observed using the 1/4-m spectrograph, but only on shots including the interaction beam. Without the interaction beam there was never any measurable signal except for the near-blackbody plasma background radiation. Typical spectra are shown in Fig. 47.8 for two cases, with the interaction beam timed (a) 0.6 ns and (b) 1.2 ns after the primary plasma-producing beams. In both cases the spectra are narrow. Drake *et al.*<sup>18</sup> reported narrow Raman spectra; their Fig. 4 shows a spectrum taken at  $10^{14}$  W/cm<sup>2</sup> of width 60 nm, and a trend towards broader spectra at higher intensities. In comparison, in case (a) of Fig. 47.8 of this article at  $10^{15}$  W/cm<sup>2</sup>, the width is only 27 nm. Although the detailed characteristics of the SRS emission will be discussed in a separate article, it should be pointed out here that the measured SRS threshold corresponds well to the collisional threshold for emission from the center of the parabolic density profile as calculated by Williams<sup>19</sup> for the present conditions.

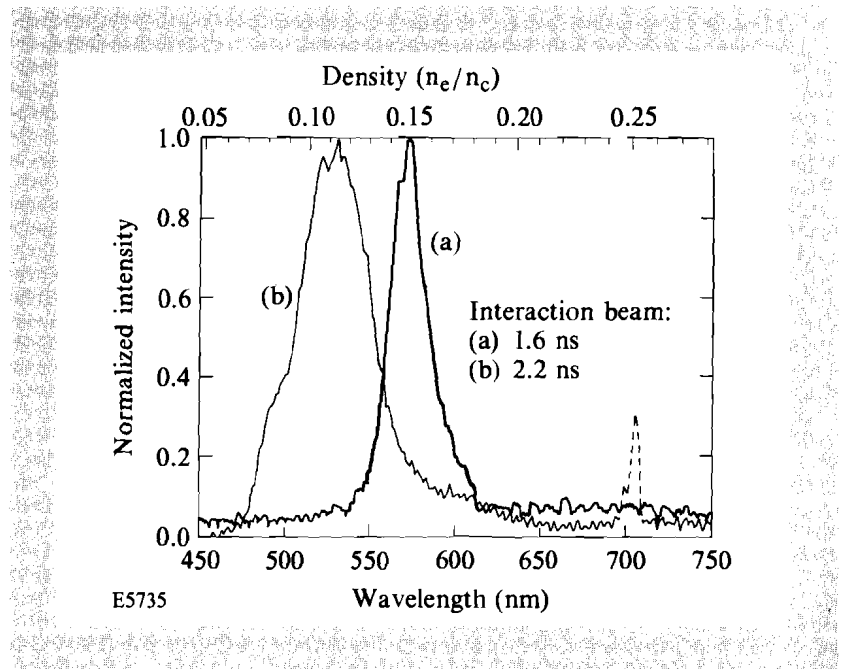


Fig. 47.8

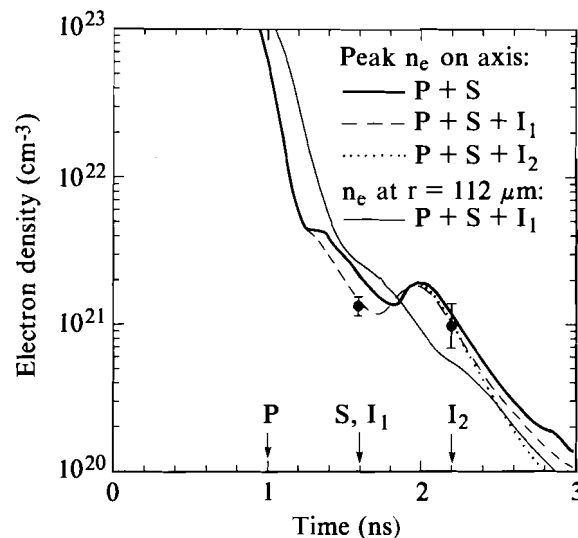
Typical stimulated Raman spectra taken for two cases with different timings of the interaction beam: (a)  $t = 1.6$  ns, the same time as the peak of the secondary heating beams; and (b)  $t = 2.2$  ns. The narrowness of these spectra strongly suggests that the Raman emission originates from the density maximum (along the  $z$  axis) and permits an accurate determination of this electron density (top horizontal scale) at the time of the interaction beam.

The narrowness of the SRS spectra, especially in case (a), implies that the emission occurs over a very narrow range of electron densities. The electron density  $n_e$  corresponding to an SRS wavelength  $\lambda_R$  is given approximately by the relation  $n_e/n_c = (1 - \lambda_0/\lambda_R)^2$ , and is shown on the density scale on top of the figure. [Here  $\lambda_0$  is the laser wavelength, and the very small temperature (Bohm-Gross) correction to the dispersion relation of the plasmons has been neglected.] From Fig. 47.5(b), the electron-density profile around 1.6 ns has a saddle point at the center of the plasma. The instantaneous SRS signal is probably dominated by emission from the saddle-point density, with some width arising from the (small) radial nonuniformity of the density profile. Variations of the saddle-point density over the duration of the interaction beam will add width to the time-integrated spectrum. However, from Fig.

47.6(b), this saddle-point density is stationary just after the peak of the interaction beam, where it has a minimum. It is thus reasonable to expect a very narrow Raman spectrum with wavelength corresponding to the minimum saddle density. This interpretation is supported by the broader spectrum observed at 2.2 ns, where the dominant source density (a true maximum rather than a saddle point) falls monotonically over the duration of the interaction beam.

The two density points obtained from Fig. 47.8 are compared with *SAGE* predictions in Fig. 47.9. Here the heavy solid curve corresponds to the dotted curve of Fig. 47.6(b), for primary and secondary beams only. However, the perturbation of the plasma by the interaction beam, though small, may be significant, and the experimental points should therefore be compared with the dashed curve (interaction beam at 1.6 ns) and the dotted curve (interaction beam at 2.2 ns), respectively. In order to give an indication of the range of densities over which Raman emission is observed, the error bars in Fig. 47.9 denote the densities corresponding to normalized SRS intensities of 0.2 taken from the spectra of Fig. 47.8. In the first case the experimental density point lies very close to the minimum in  $n_e(t)$ , as expected. In the second case the SRS emission comes predominantly from densities in the range  $0.075-0.15 n_c$ , values close to the predicted densities around the time of the interaction beam. In this case it is reasonable to associate the peak of the Raman spectrum with the peak of the interaction beam, since the Raman emission is a strongly nonlinear function of the laser intensity. However, it should be cautioned that the peak of the Raman spectrum does not necessarily give a precise measurement of the peak plasma density at the time of the interaction beam, since Landau damping at lower densities and inverse-

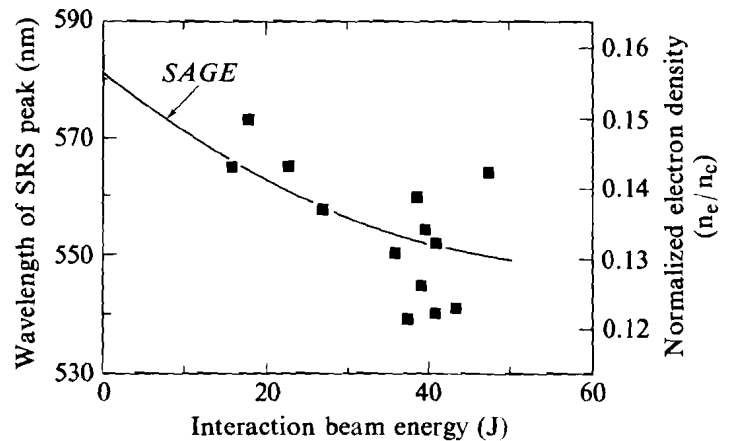
Fig. 47.9  
 Maximum on-axis electron density as a function of time, as calculated by *SAGE*, for no interaction beam (thick solid curve), for the (50-J) interaction beam located at 1.6 ns (dashed curve), and for the interaction beam at 2.2 ns (dotted curve). The thin solid curve gives the electron density at  $r = 112 \mu\text{m}$  and  $z = z_{\text{mid}}$ . In all cases the primary (P) and secondary (S) beams are on. Experimental density data, derived from the peaks of the spectra shown in Fig. 47.8, are plotted at the time of the interaction beam. The error bars indicate the density spread corresponding to Raman intensities 20% of the respective maxima in Fig. 47.8. The point at 1.6 ns should be compared with the dashed curve and that at 2.2 ns with the dotted curve.



RUNS 2343, 54, 56  
 TC2941

bremsstrahlung absorption at higher densities could affect the measured spectra.<sup>18</sup> Figure 47.9 also gives the electron density history at a point 112  $\mu\text{m}$  off axis (thin curve); this illustrates that the center of the plasma is a saddle point before 1.8 ns and a maximum thereafter.

In order to examine the extent to which the interaction beam (at 1.6 ns) perturbs the plasma, the density was obtained from Raman spectra such as that of Fig. 47.8 for various interaction-beam energies. The results are plotted in Fig. 47.10, together with *SAGE* predictions obtained from the minima of curves such as the dashed curve of Fig. 47.9. The experimental trend is in good agreement with simulations, and is understood simply on the basis that plasmas that are heated more, expand faster. It is also seen that the perturbation in the plasma density induced by the interaction beam is minimal. On the basis of simulations (compare the solid and dotted curves of Fig. 47.9), even less perturbation of the background plasma is expected when the interaction beam irradiates the lower-density plasma at 2.2 ns.



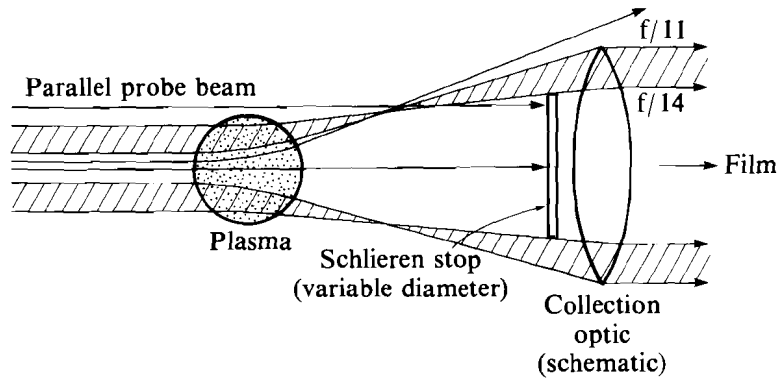
RUNS 2343, 54-60  
TC2942

Fig. 47.10

Wavelength of the SRS peak and the corresponding electron density as a function of interaction beam energy on target. In all cases the primary and secondary beams are on and the interaction beam is located at 1.6 ns. The calculated density corresponds to the minimum of curves such as the dashed curve of Fig. 47.9.

### 3. Electron Density Evolution via Schlieren Photography

The configuration for Schlieren photography used in these experiments is shown schematically in Fig. 47.11. An image of the plasma is produced using just those rays of the probe beam that are bent enough to miss the central circular stop of the QUESTAR (here represented by a simple lens with a central stop) but not so much that they miss the edge of the lens. This straightforward model is incorporated into *TRACER-3*, a 3-D geometric-optics ray-tracing postprocessor to *SAGE*. In practice, diffractive effects can complicate the image, but no attempt has been made to model these effects. *TRACER-3* calculates the trajectories of a 2-D grid of probe rays, typically 30–50 in each dimension, and then generates the boundaries of the Schlieren image simply as contours of equal deflection angle.



TC2889

Fig. 47.11

Geometric optics illustration of Schlieren image production using a short-pulse probe beam incident on the target. The size of the primary QUESTAR mirror, represented here by a lens, corresponds to  $f/11$ . The minimum size of the central Schlieren stop is equal to the diameter of the secondary QUESTAR mirror, corresponding to  $f/50$ . The central stop was sometimes enlarged to  $f/14$  in order to produce narrow images of the expanding plasma for multiple exposures.

Two series of Schlieren photographs were obtained. In the first series, the expansion phase of the plasma was investigated quantitatively by using the pulse-stacked probe beam with an enlarged central stop in front of the QUESTAR microscope. Thus only rays with refraction (or scattering) angles lying in the narrow range between the  $f/14$  and  $f/11$  focal cones were admitted for image construction. Since the pulses were produced using two 70% mirrors, the energy of each successive pulse was reduced by a factor of two. As a result, the experimental Schlieren pictures only allowed approximately three reasonably distinct exposures. Typical Schlieren images obtained in this way, for three shots with just the primary and secondary beams on, are shown in Fig. 47.12(a)–(c). A problem arises in some of the images because of imperfect centering of the unperturbed (unrefracted) beams on the target and the central aperture stop on the QUESTAR. This, along with a possible slight misalignment of the pulse-stacking mirrors and the steep film-response curve, can easily account for the clearly discernible intensity asymmetries in the images and the apparent loss of portions of some of the rings. However, the originals clearly reveal symmetric structures that can be quantitatively compared with simulations of these images [Fig. 47.12(d)–(f)].

The three Schlieren photographs in Fig. 47.12 were taken with different timings of the probe beam relative to the primary and secondary beams. The relative timings between the primary and secondary beams, and between each probe pulse, are known to high accuracy, but the relative timing between the primary and probe beams (which derive from different oscillators) is less well known. The corresponding times shown in Fig. 47.12 are therefore inferred from the simulations. The simulated images of Fig. 47.12 are reproduced on the same scale as the experimental images, and the close correspondence is easy to demonstrate. The agreement between predictions and experimental observations is indeed very good, giving confidence that the simulations replicate the various plasma parameters with acceptable accuracy.

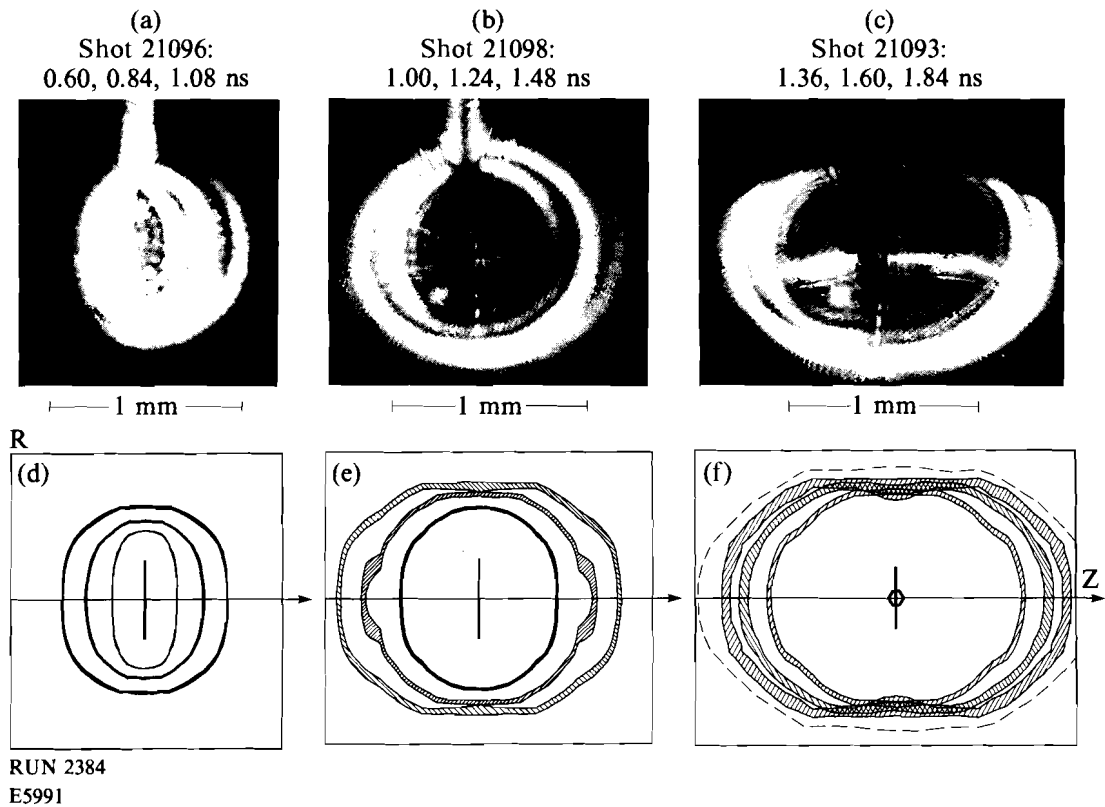


Fig. 47.12

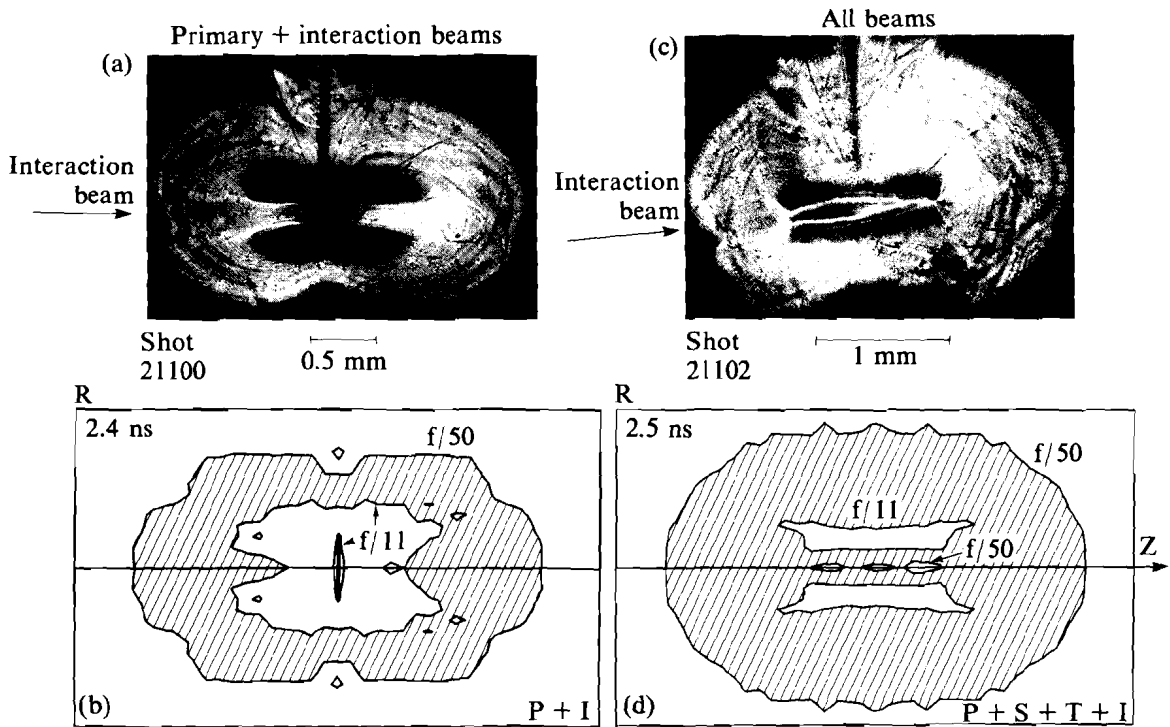
Figures 47.12(a)–47.12(c) show multiple Schlieren images of the expanding plasma, obtained using a  $\sim 20$ -ps, 527-nm probe beam containing a series of pulses of decreasing intensity and separated by 240 ps. In each case the target was irradiated with just the primary and secondary beams. The orientation of the images is consistent with Fig. 47.1, i.e., the horizontal ( $z$ ) axis is the axis of cylindrical symmetry. A large  $f/14$  Schlieren stop was used in conjunction with the  $f/11$  collection optics so that each image corresponds to a narrow region of the plasma. The three shots correspond to different timings of the probe beam, ranging from early (a) to late (c). Figures 47.12(d)–47.12(f) show corresponding images predicted by *SAGE* and *TRACER-3*, on the same scale. The dashed curve in (f) is the contour of  $n_e/n_c = 0.005$  at the latest time (1.84 ns).

The images of Fig. 47.12 are, of course, contours of deflection angle and not of electron density. However, simulations show that the density contours generally have a similar shape, as illustrated by the dashed curve in Fig. 47.12(f). Thus, the evolution of the Schlieren ring provides a useful visual representation of the evolution of the plasma. Figure 47.12 shows the evolution from an oblate spheroidal plasma shortly after plasma formation, to a spherical plasma, and finally to a prolate spheroidal plasma. Greater expansion along the axial (horizontal) direction than the radial direction is clearly evident.

#### 4. Schlieren Photography in the Presence of the Interaction Beam

A very limited set of experiments was carried out taking Schlieren images

of the plasma in the presence of the interaction beam. For these shots the secondary QUESTAR mirror was employed as the central Schlieren stop, corresponding to  $f/50$ , and a single probe pulse was used. Figure 47.13 shows two such images, one for the case of no secondary or tertiary heating beams, when the interaction beam was fired into a relatively cold plasma [ $T_e \geq 300$  eV, see curve P of Fig. 47.6(a)], and one with all beams on, secondary and tertiary beams included. The interaction beam peaked at 2.2 ns in both cases. The probe beam image was taken at  $\sim 2.2$ – $2.4$  ns, although, as previously discussed, there is some uncertainty as to the exact relative timing. A comparison of the two cases shows that the hydrodynamic evolution of the plasma in response to the interaction beam is strongly dependent on whether the preformed plasma is hot or cold. The simulated density and temperature profiles at the peak of the interaction beam are shown in Figs. 47.5(c) and 47.5(d).



E5990

Fig. 47.13

Experimental and simulated Schlieren images of the long-scale-length plasma around the time of the interaction beam (2.2 ns), in 527-nm light deflected between  $f/50$  and  $f/11$ . Left column: primary and interaction beams only; right column: all beams on. Figs. 47.13(b) and 47.13(d) show simulated images at 2.4 ns and 2.5 ns, respectively. In the simulated images, the shaded areas correspond to what would be seen experimentally [bright areas of Figs. 47.13(a) and 47.13(c)]. All images are on the same scale. The interaction beam enters from the left in the experiment, and from the right in the simulations (which are approximately left-right symmetric).

The first image of Fig. 47.13 includes a bright central feature that appears to follow the interaction beam through best focus, where it has the appropriate diameter ( $d_{90} = 160 \mu\text{m}$ ). While it is tempting (and justified to a certain extent) to interpret the image in terms of the interaction beam digging a channel through the preformed plasma, it must be remembered that the Schlieren image gives information about rays that have been deflected (or scattered) a certain amount by the density profile, which in turn has been perturbed in response to the interaction beam. Given that it takes the plasma a finite time to expand after being heated by the interaction beam, the best time to probe may be a little after the peak of the interaction beam.

A simulated Schlieren image for this case is shown in Fig. 47.13(b) at 2.4 ns, the time at which closest correspondence is obtained. The shaded area in the simulated image corresponds to the region between the  $f/50$  and  $f/11$  contours and should correspond to the bright portions of the experimental image. The size and shape of the outer  $f/50$  contour agree well with experiment, consistent with the observations of Fig. 47.12. The central region is obscured by refraction but has almost broken up into two off-axis lobes, subject to strong radial refraction, and most probe rays passing near the  $z$  axis are collected. [There is a small region near the center, around the singular ray that passes undeflected through the center of any plasma with exact cylindrical symmetry, where the ray deflection is less than  $f/50$ , but this region is too small to be significant.] The predicted channel size is, however, somewhat bigger than that observed. It is clear that a series of probe images with precisely known absolute timing would enable an improved understanding to be obtained of the hydrodynamic response of the preformed plasma to the interaction beam.

One feature of the experimental image [Fig. 47.13(a)] that is well explained by the simulations is the break in the channel in the center. This is due to absorption of the probe beam in the cold plasma [ $<400$  eV, see Fig. 47.5(d)] surrounding the channel: at the center of the plasma the probe transmission is calculated to be less than 5%.

The experimental image also shows a number of features not modeled. The outer edge shows a slight left-right asymmetry and a more marked up-down asymmetry, which are caused by a slight misalignment of the probe beam and the QUESTAR optic axes. Since the  $f/50$  Schlieren stop, i.e., the secondary mirror of the Cassegrainian optics, subtends a half-angle of 10 mrad, the observed 3–6-mrad alignment error makes a 30%–60% change in the  $f$  number indicated by the outer edge. There is also a small left-right asymmetry in the intensity of the image (hard to see in the reproduction) most likely due to a small miscentering of the probe beam on the plasma.

The apparent bend in the interaction beam channel (of a few degrees) is probably best explained by imperfect cylindrical symmetry of the plasma that turns the plasma itself into a distorting optical component. Also apparent

in Fig. 47.13(a) is the influence of the stalk that fills out what would otherwise have been a cusp. The cusp, visible in the lower part of this figure, is presumed to be associated with the least-well-irradiated portions around the edge of the target, and is not seen clearly in the simulation, although a cusp-like feature is present in Fig. 47.13(b). This may arise from a lack of adequate spatial resolution in *SAGE* in the vicinity of the edge of the target, but the cusp could reflect the azimuthal asymmetry of the irradiation pattern of the primary beams previously discussed, wherein four regions in the target plane receive less than the average irradiation intensity and expand slower than average. Here it should be noted that the probe beam passes through the target plane at  $45^\circ$  to the axes of the elliptical focal spots; thus two of the under-irradiated regions correspond in location to the top and bottom of the Schlieren image.

The second image [Fig. 47.13(c)] is qualitatively different from the first image. The dark central region is much smaller, almost rectangular in shape, and contains a couple of long, thin, bright regions that cannot reasonably be associated with a beam channel or filaments. A simulation of the Schlieren image at 2.5 ns is shown in Fig. 47.13(d). The outer border again corresponds well with the size and shape of the experimental image. The central feature, however, evolves in a manner consistent with a plasma that is expanding but not significantly perturbed by the interaction beam. (A small perturbation to the experimental image may be seen at the input side.) At 2.2 ns, simulations show that the whole central region is obscured, aside from a small inner area around the singular ray as discussed above. The inner shaded region expands, and by 2.5 ns [Fig. 47.13(d)] has merged with the outer shaded region. This leaves two long, thin, unshaded (i.e., dark) regions off axis where the probe rays are refracted outside the collection optic, and a dark region on the axis (broken up into three islands in the simulation) where rays are not refracted enough to miss the Schlieren stop. All these features are seen at least qualitatively in the experimental image, and quantitatively with respect to their axial extent. In addition, probe-beam transmission through the (hot) plasma is very high, so that no dark central region is either expected or seen in the second experimental image.

Figure 47.13 clearly shows that optical probing can be used to diagnose the significantly different hydrodynamic responses of the plasma to the interaction beam in the two cases. Since the plasma expansion is strongly related to electron thermal transport, particularly in the radial direction, it is also evident that optical-probing diagnostics can potentially provide insight into issues of 2-D thermal transport. *SAGE* uses a standard flux-limited transport model,<sup>17</sup> where the heat flux is directed down the temperature gradient and has a magnitude reduced from the classical Spitzer-Härm<sup>20</sup> value according to a flux limiter<sup>21</sup>  $f$ , chosen to be 0.04 for these simulations. The evolution of the preformed plasma in the simulations presented here is in fact rather insensitive to  $f$ , since the temperature scale lengths generated are rather long and the heat flow is close to classical; however, steeper temperature gradients are induced in the cold plasma by the tightly focused interaction beam, as seen in Fig. 47.5(d).

It must also be recognized that the flux-limiter model, which has been very successfully used to calculate laser absorption in the coronas surrounding solid targets where both temperature and density gradients are very steep,<sup>12,22</sup> is not necessarily appropriate for the long-scale-length underdense plasmas under consideration here. In addition, recent 2-D Fokker-Planck simulations carried out by Epperlein *et al.*<sup>23</sup> have shown that the heat flux can be reduced below classical in situations where the temperature perturbation scale length is small, even if the temperature gradient scale length ( $T_e/l\nabla T_e$ ) is long. Such a reduction in heat flux could make thermal self-focusing dominate over ponderomotive self-focusing in many circumstances of interest.<sup>24</sup> At present it is not known experimentally whether the cold plasma is actually as perturbed as *SAGE* predicts [Fig. 47.5(d)], or whether the hot plasma is as unperturbed as predicted [Fig. 47.5(c)], although the experimental data of Fig. 47.10 appears to support *SAGE* predictions for the perturbation to the plasma induced by the 1.6-ns interaction beam. The long-scale-length plasmas produced on OMEGA thus provide a valuable test-bed for studying both 2-D thermal transport and self-focusing.

### Conclusion

A novel scheme employing time-staggered beams from the multibeam OMEGA laser system has been used to produce mm-size, long-scale-length plasmas, whose temperatures can be kept at or above 1 keV over an extended period of time during the expansion phase. Such plasmas are of great interest to laser fusion, since they permit many interaction processes to be conveniently studied and they allow the determination of many important parameters such as threshold and saturation intensities. The present scheme has significant advantages of flexibility and the effective use of available laser energy in comparison with some previously used schemes.

These plasmas are formed by a set of 351-nm primary beams focused at near-normal incidence and at low intensity onto thin, 600- $\mu\text{m}$ -diam CH targets, and heated by secondary and tertiary beams focused at oblique incidence. An interaction beam, incident along the initial target normal, is focused at high intensity ( $\sim 10^{15}$  W/cm<sup>2</sup>) into the preformed plasma and can, with appropriate timing, interact with plasmas of various maximum densities. In these experiments central densities around  $n_c/8$  have been accessed at the time of the interaction beam, with the scale length, defined as the FWHM of the density profile, around 0.8 mm.

These plasmas have been diagnosed in three ways. Time-resolved spectroscopic measurements of the ratio of aluminum Ly $\beta$  and He $\beta$  lines have indicated electron temperatures in the range 1.0–1.5 keV for a time just under 1 ns. Time-integrated Raman spectra have given a precise diagnosis of the central density around the peak of the interaction beam, and the relative widths of these spectra for different interaction beam timings have indicated different phases in the plasma expansion. The variation with interaction beam energy of the central density obtained from the Raman spectra has provided, probably for the first time, a quantitative measure of the perturbation produced in the plasma by the interaction beam. Finally, Schlieren

imaging of the plasma using a 20-ps, 527-nm probe beam has, through comparison with 2-D hydrodynamic simulations, provided understanding of the 2-D evolution of the plasma.

The characterization of these plasmas is obviously an essential first step toward their use for the study of nonlinear processes. Here the 2-D plasma expansion and the evolution of the electron temperature and density have all been found to be in good agreement with the predictions of the 2-D hydrodynamic code *SAGE*. This agreement permits increased confidence in the predictive capabilities of hydrodynamic codes such as *SAGE* for future experiments.

A number of interaction-physics experiments have been carried out on these plasmas and yielded interesting results. For example, the experimental SRS thresholds are, for the first time, in excellent agreement with analytic theory, within a factor of two, rather than a factor of  $\sim 10$  below the theoretical predictions as is often found. Also, significantly lower SRS signal intensities are found when smoothing by spectral dispersion (SSD<sup>10</sup>) is implemented on the laser. These results will be reported in detail elsewhere.

Several directions for future work are suggested by the results reported here. Using the beams of the present OMEGA system, and optimizing the focusing and timing of the tertiary beams, it should be possible to extend the range of plasmas accessible to include hotter plasmas and/or plasmas with longer scale lengths and lower densities. By establishing an absolute timing for the short-pulse probe beam, it should be possible to confirm (or constrain) the hydrodynamic modeling of the expansion phase and follow more closely the evolution of the plasma subsequent to irradiation by the interaction beam. This could give insight into the lateral transport of energy deposited by the interaction beam and enable comparison to be made with Fokker-Planck modeling. Finally, by using a 263-nm probe instead of, or in addition to, the 527-nm probe, higher plasma densities will become accessible and it may be possible to study the self-focusing of 351-nm laser light under conditions relevant to laser-fusion reactors.

#### ACKNOWLEDGMENT

This work was supported by the U.S. Department of Energy Office of Inertial Confinement Fusion under agreement No. DE-FC03-85DP40200 and by the Laser Fusion Feasibility Project at the Laboratory for Laser Energetics, which is sponsored by the New York State Energy Research and Development Authority and the University of Rochester.

#### REFERENCES

1. D. W. Phillion *et al.*, *Phys. Fluids* **25**, 1434 (1982); E. M. Campbell *et al.*, *Appl. Phys. Lett.* **43**, 54 (1983).
2. D. W. Phillion *et al.*, *Phys. Rev. Lett.* **49**, 1405 (1982); E. M. Campbell *et al.*, in *Laser Interaction and Related Plasma Phenomena*, edited by H. Hora and G. H. Miley (Plenum, NY, 1984), Vol. 6, p. 545; R. E. Turner *et al.*, *Phys. Rev. Lett.* **54**, 189 (1985); R. E. Turner *et al.*, *Phys. Rev. Lett.* **57**, 1725 (1986); J. A. Tarvin *et al.*, *Laser and Particle Beams* **4**, 461 (1986); R. P. Drake *et al.*, *Phys. Fluids B* **1**, 1089 (1989).

3. R. P. Drake *et al.*, *Phys. Fluids* **31**, 1795 (1988).
4. R. P. Drake *et al.*, *Phys. Rev. Lett.* **60**, 1018 (1988); R. P. Drake *et al.*, *Phys. Rev. A* **39**, 3536 (1989).
5. M. J. Herbst *et al.*, *Phys. Rev. Lett.* **52**, 192 (1984); J. A. Stamper *et al.*, *Phys. Fluids* **28**, 2563 (1985); J. H. Gardner *et al.*, *Phys. Fluids* **29**, 1305 (1986).
6. H. Figueroa *et al.*, in *Laser Interaction and Related Plasma Phenomena*, edited by H. Hora and G. H. Miley (Plenum, NY, 1984), Vol. 6, p. 527; H. Figueroa *et al.*, *Phys. Fluids* **27**, 1887 (1984); O. Willi, P. T. Rumsby, and Z. Lin, in *Laser Interaction and Related Plasma Phenomena*, edited by H. Hora and G. H. Miley (Plenum, NY, 1984), Vol. 6, p. 633.
7. S. H. Batha, D. D. Meyerhofer, A. Simon, and R. P. Drake, *Phys. Fluids B* **3**, 448 (1991).
8. O. Willi *et al.*, *Opt. Commun.* **70**, 487 (1989); O. Willi *et al.*, *Phys. Fluids B* **2**, 1318 (1990); C. Labaune *et al.*, in *Laser Interaction with Matter*, edited by G. Verlade, E. Minguez, and J. M. Perlado (World Scientific, Singapore, 1989), p. 185; S. D. Baton, C. Labaune, and J. L. Lacaze, *Opt. Commun.* **74**, 195 (1989).
9. Y. Kato *et al.*, *Phys. Rev. Lett.* **53**, 1057 (1984); LLE Review **33**, 1 (1987).
10. S. Skupsky, R. W. Short, T. Kessler, R. S. Craxton, S. Letzring, and J. M. Soures, *J. Appl. Phys.* **66**, 3456 (1989).
11. R. S. Craxton and R. L. McCrory, LLE Laboratory Report 99, Rochester, NY (1980).
12. R. S. Craxton and R. L. McCrory, LLE Laboratory Report 108, Rochester, NY (1980).
13. J. E. Balmer, T. P. Donaldson, W. Seka, and J. A. Zimmermann, *Opt. Commun.* **24**, 109 (1978); J. Delettrez, D. K. Bradley, P. A. Jaanimagi, and C. P. Verdon, *Phys. Rev. A* **41**, 5583 (1990); D. K. Bradley, T. Boehly, D. L. Brown, J. Delettrez, W. Seka, and D. Smith, in *Laser Interaction and Related Plasma Phenomena*, edited by H. Hora and G. H. Miley (Plenum, NY, 1991), Vol. 9, in press.
14. B. L. Henke and P. A. Jaanimagi, *Rev. Sci. Instrum.* **56**, 1537 (1985).
15. R. Epstein, S. Skupsky, and J. Delettrez, *J. Quant. Spectrosc. Radiat. Transfer* **35**, 131 (1986).
16. QUESTAR Corporation, New Hope, PA 18938.
17. R. S. Craxton and R. L. McCrory, *J. Appl. Phys.* **56**, 108 (1984).
18. R. P. Drake *et al.*, *Phys. Fluids B* **1**, 2217 (1989).
19. E. A. Williams, in *LLNL Laser Program Annual Report 1985*, Lawrence Livermore National Laboratory Report, UCRL 50021-85, pp. 2-46 (1985).